7-2021

A Spectral Component Analysis of Repeating FRB121102

Zachary Diermyer
zrd7527@rit.edu

A Spectral Component Analysis of Repeating FRB121102

M.S. *Master of Science*

in Astrophysical Sciences and Technology

Zachary Diermyer

School of Physics and Astronomy

Rochester Institute of Technology

Rochester, New York

July 2021

ASTROPHYSICAL SCIENCES AND TECHNOLOGY
COLLEGE OF SCIENCE
ROCHESTER INSTITUTE OF TECHNOLOGY
ROCHESTER, NEW YORK

CERTIFICATE OF APPROVAL

M.S. DEGREE THESIS

The M.S. Degree Thesis of *Zachary Diermyer* has been examined and approved by the thesis committee as satisfactory for the thesis requirement for the M.S. degree in Astrophysical Sciences and Technology.

Dr. Andrew Robinson, Committee Member

Dr. Michael Richmond, Committee Member

Dr. Michael Lam, Thesis Advisor

Date

A Spectral Component Analysis of Repeating FRB121102

By

Zachary Diermyer

A dissertation submitted in partial fulfillment of the requirements for the degree of M.S. in Astrophysical Sciences and Technology, in the College of Science, Rochester Institute of Technology.

July, 2021

Approved by

Dr. Andrew Robinson	Date
Director, Astrophysical Sciences and Technology	

Abstract

Fast Radio Bursts (FRBs) are extremely luminous, millisecond duration radio pulses of unknown origin. While many FRBs are transient events, a few sources are confirmed to be the progenitor of multiple bursts. These "repeaters" offer an extraordinary chance to study the properties of mysterious FRB signals. The FRB121102 source was the first repeater to have ever been discovered and it has since provided us with a wealth of data to be analyzed. A unique feature of repeaters, including FRB121102, is the presence of a multicomponent burst structure. This is a phenomenon where individual portions of the burst are separated in time. Understanding the true fraction of FRBs which contain a multicomponent structure will place limitations on the physical mechanisms which can potentially emit the bursts. We investigate this feature within the Breakthrough Listen data of FRB121102. Breakthrough Listen recorded an observation that detected 21 FRBs in one hour, making it a great source of uniform data. Our analysis compares the shapes of multicomponent and single-component bursts within the Breakthrough Listen data set. We measure fluence distribution shape using statistical moments. This process is original work which provides a new method of analysis for FRB research. Through artificial reduction of the signal-to-noise ratio of multicomponent bursts, we observe how their shape changes compared to single-component bursts. This demonstrates the potential for multicomponent burst structure to be "washed out" by noise, making some FRBs appear as single-component to the observer. We assert that the true fraction of multicomponent bursts could potentially be larger than observed.

Contents

List of Figures

List of Tables

Chapter 1

Introduction

1.1 The Fast Radio Burst Phenomenon

Fast Radio Bursts (FRBs) have been one of the greatest mysteries of radio astronomy since their discovery by Duncan Lorimer in 2007 [1]. The first discovered FRB, named the "Lorimer Burst", can be seen in figure 1.1. The defining properties of all FRBs [1] observed thus far are extremely large dispersion measures (DMs) and millisecond duration bursts. Dispersion is a phenomenon which only significantly effects the radio end of the electromagnetic spectrum. Lower frequency radio waves have delayed times of arrival (TOA). This is caused by refraction within the medium they travel through, which is wavelength dependent. DM is a value which represents the magnitude of this delay, by quantifying the electron density along the line of site to the source. The greater the DM, the more medium travelled through and the greater [2] the distance to the source. The large FRB DMs, which are usually of order $\sim$100s $\frac{\text{pc}}{\text{cm}^3}$ and in some cases $\sim$1000s $\frac{\text{pc}}{\text{cm}^3}$ [12], indicate that these bursts are extragalactic in origin. Unless the observer's line of sight passes through the galactic center, the Milky Way contribution to DM is normally $\leq$100 $\frac{\text{pc}}{\text{cm}^3}$. Figure 1.2 shows the ratio of some observed FRB DMs to the expected Milky Way contribution along the respective lines of sight.

Due to recent advancements in radio telescope technology, some FRB sources have been

[1] This is with the exception of SGR1935+24, which will be discussed in detail in a later section.

[2] This is not always the case. Overdense and underdense regions make DM-Distance relations very uncertain. However, the extremely large DMs of FRBs are highly unlikely to be from the Milky Way alone.

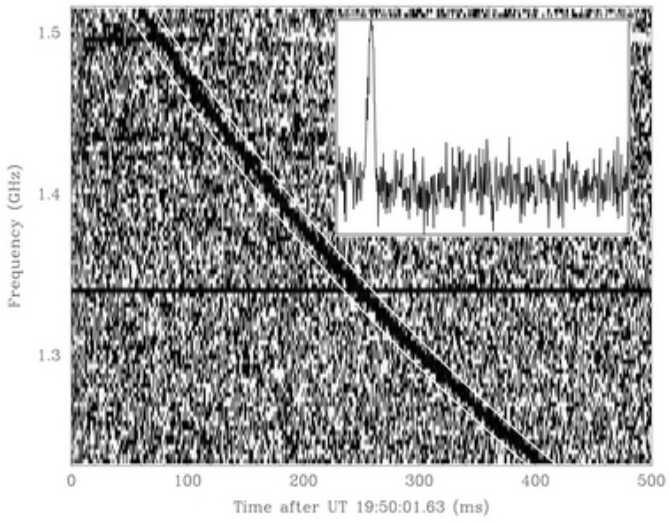

Figure 1.1: Dynamic spectrum of the first FRB ever discovered, named the Lorimer Burst. The horizontal axis is time, the vertical axis is frequency, and the shading represents intensity. Duncan Lorimer found the burst while searching through archival radio data. The dark curve is the FRB, which went unnoticed during observations. The iconic dispersion sweep can easily be seen, indicating the large DM of the source (figure 2, Lorimer et al. [1]).

localized to host galaxies. With radio telescopes around the world continuing to improve at a rapid pace, there will be many more localized FRBs in the near future. At the time of this writing there are 14 localized FRB sources and over 600 FRB detections published on arXiv according to the FRB Community Newletter [3]. A full list of FRBs with relevant observational properties can be found at the FRB Catalogue [4] [13]. The CHIME radio telescope alone claims to have detected over one thousand FRBs that have yet to be published [2]. The field of FRB research has grown immensely since the discovery of the Lorimer Burst. However, despite continued debate, the progenitor of these bursts remains unknown. The goal of our research is to discover clues which may help lead to a conclusion about what object creates FRBs. Later sections will discuss the best potential candidates.

[3] http://hosting.astro.cornell.edu/research/frb/news/
[4] https://www.frbcat.org/

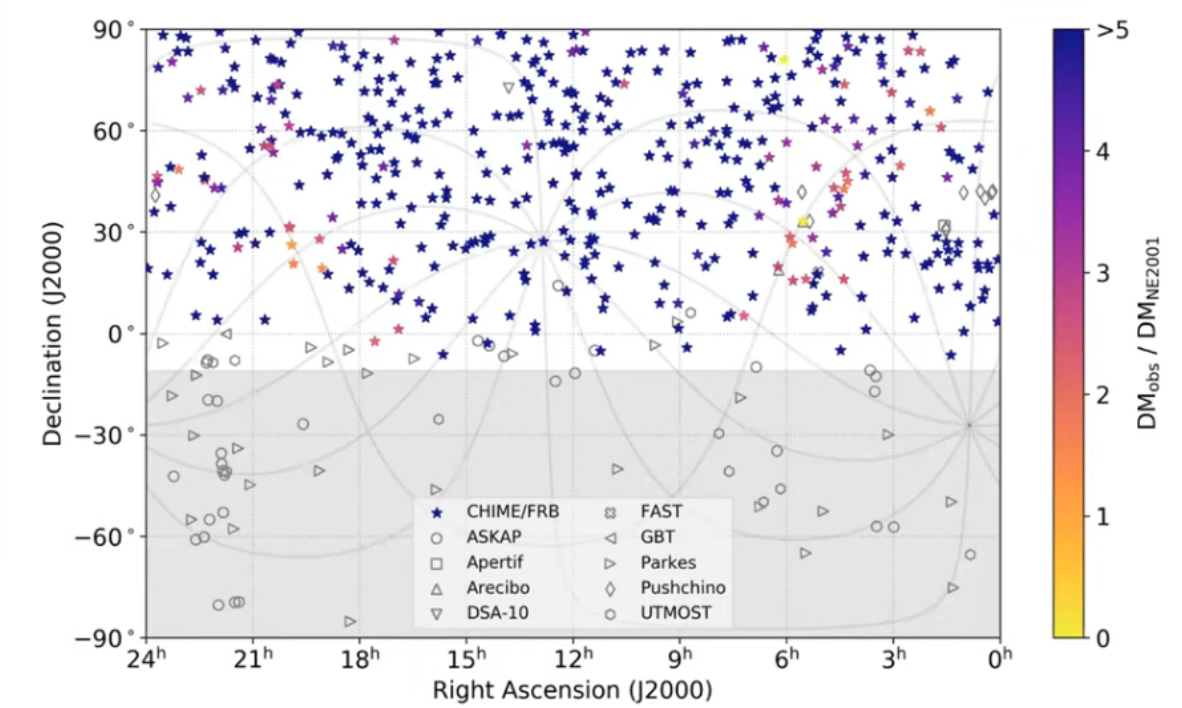

Figure 1.2: Sky map highlighting CHIME telescope FRB detections (FRB2020 session 2, Pleunis [2]). The color scale represents the ratio of observed FRB DM to the predicted Milky Way DM contribution [3]. It is clear that most FRBs have very large DMs.

1.2 Common FRB Properties

FRBs are millisecond duration bursts of radio emission. They have been observed in frequencies of ∼100s of MHz [10], [14], [15] to ∼8 GHz [16]. This corresponds to an approximate wavelength range of 2 meters to 4 centimeters. FRBs are also very luminous. The estimated isotropic energy output at the source of FRB121102 is $\sim 10^{34} \frac{\text{erg}}{\text{s Hz}}$ for each burst [17]. If an FRB source were to output this energy for one second, it would be nearly 100 times the total energy [5] released by the sun over the course of an entire year!

FRB sources were originally thought to be exclusively transient events. Bursts would be detected by chance during radio observations and no repetitions were observed. Theories surrounding FRBs often disagreed over the fundamental assumption of repetition. Some claimed a cataclysmic event such as supernovae produced these bursts, explaining why no repetitions

[5] Assuming an FRB spanning 1 GHz in bandwidth and a solar luminosity of 3.846×10^{26}W

were found from any sources. All of this changed in 2012 upon the discovery of the first repeating FRB, FRB121102. Observations using the Arecibo Observatory showed multiple bursts originating from the same sky location and with the same DM [17]. More repeating FRB sources were discovered since then and there are currently 24 sources known to repeat (FRB Catalogue).

At present, a strong debate exists over the idea that all FRB sources repeat. Because there are numerous examples of repeating FRB sources (repeaters), it is clear that all FRBs cannot be explained by a cataclysmic, singly occuring event. It is also likely that many sources which only have one observed burst (apparent non-repeaters) could repeat on very long timescales. However, there are clear differences between repeaters and non-repeaters. The repeaters are longer duration, having bursts which can last tens of milliseconds, whereas non-repeater bursts are generally a maximum of one to two milliseconds in duration [2]. Repeaters also show a component structure in some of their bursts, which is a major focus of this work. Finally, some repeaters have been associated with something called a pseudo-periodicity. A repeater known as FRB20180916B has active phases during which multiple bursts are detected over the course of a few hours. These active phases occur consistently every 16.3 days [18]. This modulation in active phases is what has become known as the psuedo-periodicity. FRB121102 is suspected to have a $\sim$154 day periodicity [19].

1.3 The Infamous FRB 121102

The Lorimer Burst, and other initial FRB detections, were all made using the Parkes Radio Telescope. This led some to question the astrophysical nature of these anomalies. The hunt was on for other telescopes to confirm that the radio bursts were real. Nearly five years after the Lorimer Burst was first discovered, Spitler et al. [20] detected a very bright radio burst with the Arecibo Radio Telescope. The unusually large DM of this detection led them to the same conclusion as Lorimer et al. [1]. They had detected an extragalactic radio burst from an unknown source. The burst showed an inverted spectrum, which is a spectrum exhibiting a positive spectral index. This was very peculiar, as all coherent emission processes (like those

of neutron stars) show a negative spectral index. This was confirmed to be an outcome of the burst detection occurring in a side lobe of the telescope. As mentioned previously, the FRB121102 [6] source is a repeater. Follow-up observations by Chatterjee et al.[17] made it the first discovered repeating FRB source, as well as the first detected with a telescope other than Parkes. Additional observations pointed towards the locations of FRBs detected by Parkes showed no repeat bursts. The FRB121102 source seemed especially strange.

FRB121102 is in fact one of the most active and energetic FRB sources in the known Universe. This has lead to its localization in a dwarf irregular galaxy at a redshift of z = 0.19273(8) and distance D = 972 Mpc [17], [21]. To date, over 200 bursts have been observed originating from FRB121102 [22]. This wealth of data has made FRB121102 the most well studied FRB source and the basis of many repeater theories.

An interesting aspect of FRB121102's environment is a continuous radio source companion, seen in figure 1.3, located near the position of the FRB source [4]. This is likely a compact object such as a black hole or neutron star. The companion may be an explanation for the extreme activity of FRB121102. This is especially the case when analyzing the unprecedentedly large rotation measure (RM) of FRB121102. Most estimates are around $10^5 \frac{\text{rad}}{\text{m}^2}$ [23], which isn't observed in any other FRB to date. The usual RM of an FRB is $\leq 100 \frac{\text{rad}}{\text{m}^2}$. RM values are dependent on the electron density and magnetic field strength along the line of sight to the source. A compact object companion would be the best explanation for the high rotation measure of FRB121102 because an extremely magnetic environment increases RM.

1.4 Structure Maximizing Dedispersion

Before analyzing radio data, they must first be dedispersed. As mentioned previously, dispersion is an effect caused by the interstellar medium (ISM) and intergalactic medium (IGM), which makes radio waves at lower frequencies lag slightly behind those at higher frequencies. It is necessary to put our data through a process of dedispersion in order to reveal the

[6] Catalogued as FRB20121102A in the CHIME/FRB Catalog (https://www.chime-frb.ca/repeaters) and Transient Name Server (https://www.wis-tns.org//), but simply referred to as FRB121102 in this writing.

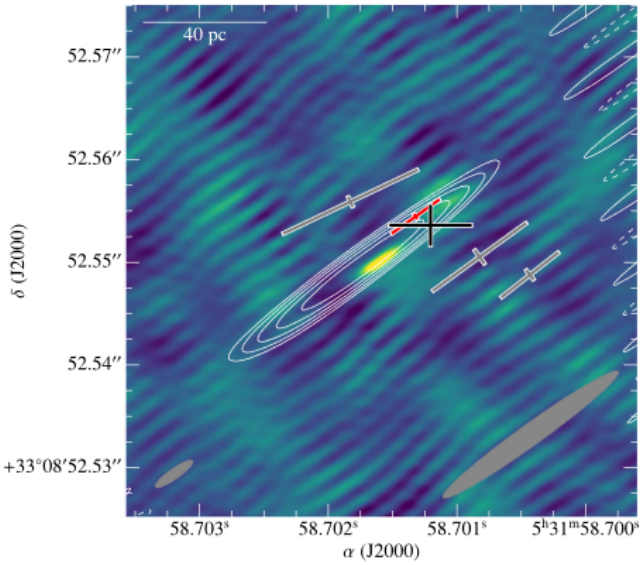

Figure 1.3: EVN radio image of FRB121102 host galaxy (figure 1, Marcote et al. [4]). The black cross is the position of the FRB source and the red line is the position of the continuous radio companion.

true structure of the signal. Dedispersion of data involves shifting the data forward in time. The amount that data is shifted is proportional to the DM and inversely proportional to the frequency squared. The diagram in figure 1.4 illustrates this process.

The standard dedispersion method will shift the data so all of the emission lines up perfectly in time, like in the leftmost panel of figure 1.4. This is called the signal to noise (S/N) maximizing dedispersion. A key aspect of Breakthrough Listen data is the observation of multi-component bursts. It was noted that there are "breaks" in time within a few of the FRBs. These breaks span many frequencies, which makes them more likely to be an attribute of the source than scattering or other noise [24]. If dedispersed to a S/N-maximizing DM value, the breaks would be slanted in time. This implies a very narrow bandwidth being emitted from the source with a constantly changing frequency. The latter scenario can be seen in figure 1.5 and is unlike anything naturally occurring, thus the multi-component FRBs are only dedispersed until the breaks align in time. This method of dedispersion is named structure maximizing dedispersion. Gajjar et al. [5] find a structure maximizing DM value of 565.0 $\frac{\text{pc}}{\text{cm}^3}$ and dedisperse all Breakthrough Listen burst snapshots to this value.

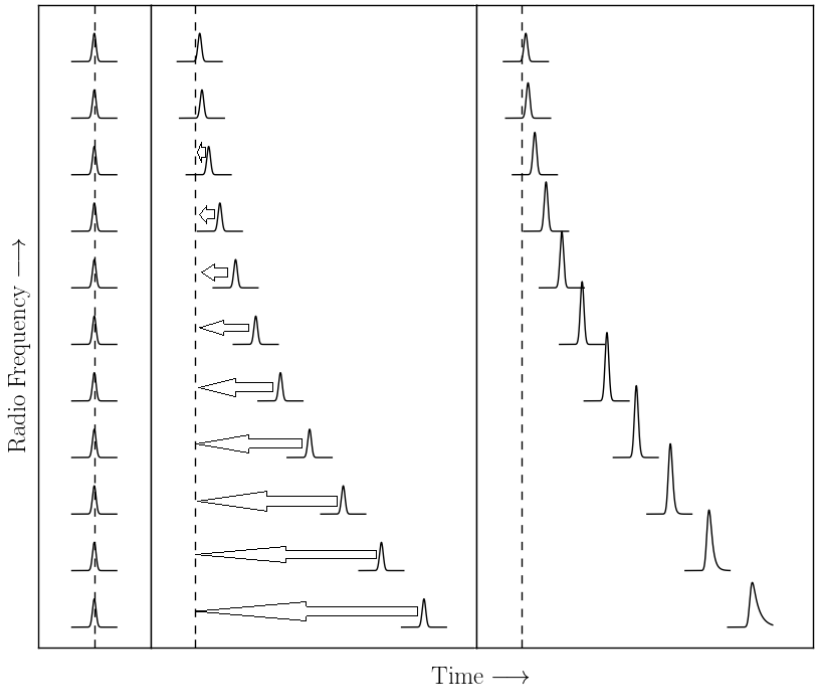

Figure 1.4: Diagram of dedispersion process. The two panels on the right show data that has not been corrected for dispersion. The leftmost panel is the dedispersed data. All frequency channels are shifted to earlier times so as to align the signal across the entire bandwidth. The rightmost panel includes an example of a pulse which has been affected by scattering at low frequencies.

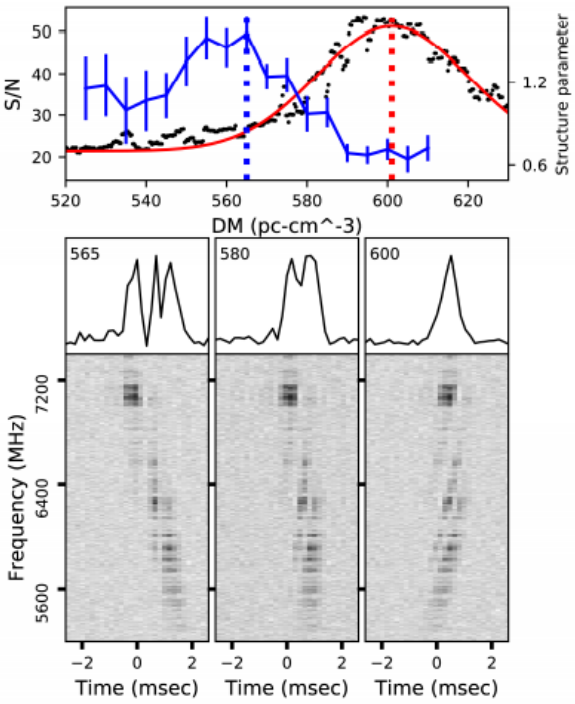

Figure 1.5: Comparison of the different DM trials used to find the optimal DM value of burst 11A (figure 1, Gajjar et al. [5]). The lower three panels are dynamic spectra showing the burst for different DM trials. Above each dynamic spectrum is the total intensity averaged over frequency, with the trial DM in the top left corner. The top panel shows burst S/N ratio (black dots and red line) as well as structure parameter values (blue line) for different DMs. The temporal breaks can be seen slanting across the FRB for a DM value of 600 $\frac{\text{pc}}{\text{cm}^3}$, the S/N maximizing dispersion value. However, using the structure parameter, the breaks can be properly aligned in time, yielding data which is more astrophysical in nature. The structure parameter is given by $\frac{1}{n}\sum_{i=0}^{n}\left|\frac{S_i - S_{i+1}}{\Delta t}\right|$ where S_i is the flux density of the ith time bin, Δt is the time length per bin, and n is the total number of time bins.

Chapter 2

FRB Theory

2.1 Proposed Spectro-Temporal Burst Structure Relationship

Since the discovery of FRBs, an incredible amount of proposed progenitors have been hypothesized. The myriad theories range from exotics, like axion stars [25] and cosmic strings [26], to the more familiar, like neutron star binaries [27] and asteroids impacting neutron stars [28]. A totally encompassing list is kept at the FRB Theory Catalogue [1]. There may very well be multiple different progenitors, given the distinctions between repeaters and non-repeaters. For example, superluminous supernovae have been ruled out as the source of repeaters but may be a source of non-repeaters. It even appears that **repeaters** may originate from multiple different sources. The relatively tame FRB20180916B has been proposed to be a neutron star with a high mass stellar companion, like those of high mass X-ray binaries [29]. Alternatively, the incredible RM of FRB121102 correlates with a source magnetic field strength which is only known to exist in magnetars and black holes [2].

In this work, we assume a compact object as the FRB121102 source. We focus on the relatively simple question of how compact objects create FRBs. The bursts we observe may be emitted directly from the source or refracted by some surrounding medium after a triggering event. The latter scenario is illustrated in figure 2.1. A potential way to answer this question is

[1] https://frbtheorycat.org/index.php/Main_Page

[2] We caution the reader not to jump to conclusions. The companion object of FRB121102 likely contributes significantly to the magnetic field strength at the source.

by analyzing the multicomponent structure observed in some FRBs. Multicomponent structure is a unique feature of repeating FRB sources. This feature is observed as parts of FRB emission being separated in time. Because the break in emission is temporal, and spans a wide frequency range, it must be caused by the progenitor. This gives us an opportunity to investigate what physical mechanisms might create an FRB. Of the 21 bursts found in the Breakthrough Listen data set, two show a clear multicomponent structure. We compare some properties of these multicomponent bursts to those of the bursts with only a single component. If properties of multicomponent bursts are significantly different from those of single component bursts, more than one physical mechanism may be needed to explain FRBs.

Rajabi et al. [6] give a potential explanation for the multicomponent structure seen in repeaters. They use the same data set as the one in our analysis and also assume a compact object (neutron star) source model. The scenario described by Rajabi et al. [6] can be seen in figure 2.1. In it, they use a neutron star trigger (energy source) and surrounding medium FRB source. In other words, the neutron star releases a burst of energy and the surrounding medium transforms it into the radio emission we observe as an FRB. This model can accurately describe the creation of multicomponent bursts. The model relies on Dicke's superradiance to explain the downward frequency drifting (sad trombone) often seen in multicomponent bursts. Dicke's superradiance is characterized by a group of quantum mechanical particles with coherent behavior. The particles act as a single quantum mechanical unit as opposed to many individual ones. Superradiance occurs in a medium moving at relativistic speeds. This effect causes narrowband processes to be emitted at multiple descending frequencies, like the downward frequency drifting seen in FRBs. If it can be shown that many bursts are intrinsically downward frequency drifting, it will be more likely that Dicke's superradiance shapes the FRBs we observe.

2.2 SGR1935+2154 and the Potential Galactic FRB

What could power radio bursts as uniquely luminous as FRBs? Compact objects have been known to be powerful radio emitters for decades. Pulsars are well studied compact objects

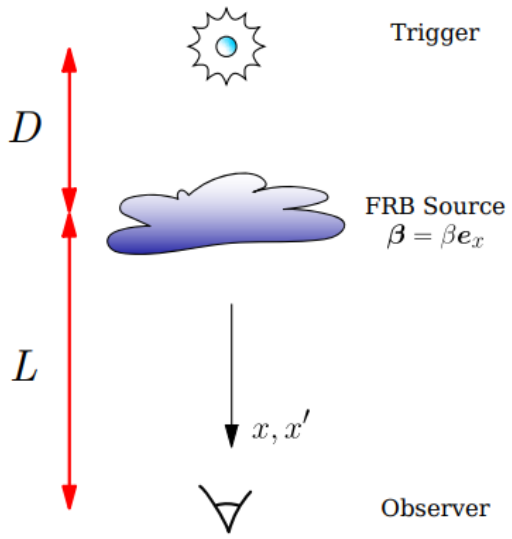

Figure 2.1: Schematic diagram of FRB creation as described by Rajabi et al. (figure 1, Rajabi et al. [6]). The neutron star trigger is a distance D from the FRB source, a surrounding medium moving at relativistic velocity with β fraction of the speed of light. We observe the FRB a distance L away from this medium.

which have radio beams originating from their magnetic poles. However, regular pulsar emission is many orders of magnitude weaker than FRBs. A young pulsar, known as the Crab pulsar, exists within our galaxy and has emitted "giant pulses" (GPs). Even Crab GPs are still far too weak to explain FRBs as can be seen in figure 2.2. Cordes et al. [30] propose "supergiant pulses" may explain some FRBs. After the localization of FRB121102, it was determined that theoretical supergiant pulses could not account for the luminosity of FRB121102 bursts.

Margalit et al. [31] suggest that young magnetars may have the proper astrophysical nature to form FRBs. Magnetars are a type of young neutron star with extremely powerful magnetic fields. They can be as powerful as 10^{15} Gauss at their surface. Magnetic fields this powerful are akin to those born from science fiction. It is unclear exactly why some neutron stars are born with this extremely strong magnetic field. Because of magnetic reconnection, the magnetic fields of magnetars are deteriorated quickly and they eventually become relatively normal pulsars.

On April 28, 2020, the galactic magnetar known as SGR1935+2154 provided radio astronomers with a gift that may answer the FRB origin question. It emitted an extremely bright

radio flare that lasted for a few milliseconds [32]. More bursts were detected during the next few days. These suspiciously similar characteristics to FRBs made SGR1935+2154 famous amongst FRB astronomers practically overnight. Its initial bright radio burst was even given the title FRB20200428 in the FRB Catalogue. The only flaw which made SGR1935+2154 bursts unable to officially be considered galactic FRBs was their energies. Bursts detected from this source were at least two orders of magnitude fainter in luminosity than the weakest extragalactic FRBs detected. There are five recorded radio bursts originating from the SGR1935+2154 source at the time of this writing. They span seven orders of magnitude in radio luminosity, as shown by the grey shaded region in figure 2.2. With a data set of brighter magnetar bursts or fainter extragalactic FRBs, magnetars would have a strong case for being considered FRB progenitors.

The search for fainter extragalactic FRBs has now become one of the most popular items on FRB astronomer's agendas. For example, Marthi et al. [33] recently observed bursts from the FRB20180916B source that are only one order of magnitude greater in energy than the SGR1935+2154 burst. Another recent publication from Majid et al. [7] claims the detection of nanosecond duration burst components, which are only slightly more energetic than the galactic magnetar burst. With luck, the FRB mystery may soon come to a close.

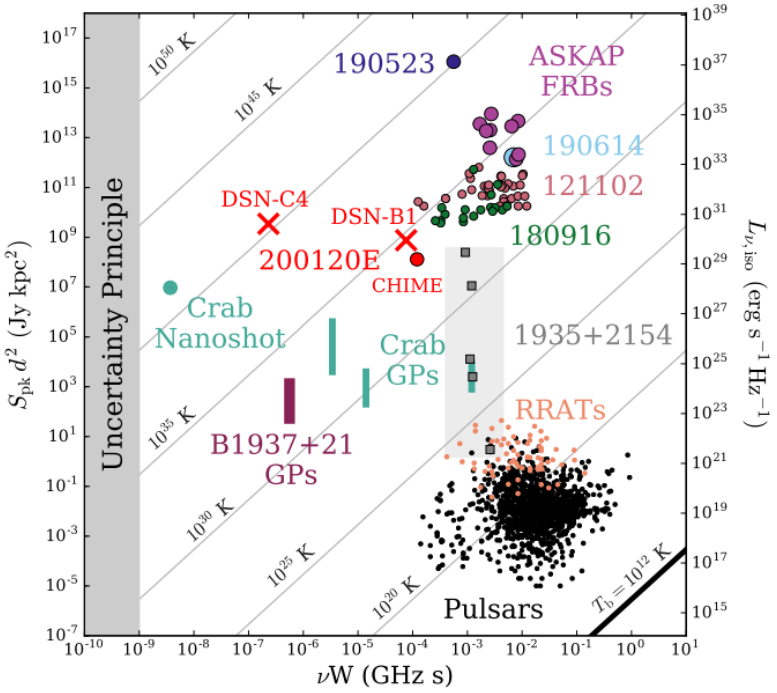

Figure 2.2: Phase space showing radio luminosity versus frequency-width of some common radio sources (figure 4, Majid et al. [7]). Diagonal lines are of constant brightness temperature. The left luminosity is the radio pseudo-luminosity whereas the right is isotropic luminosity at a given frequency. The dark grey shaded region represents signals which are too short in duration to observe because of the uncertainty principle. The recently observed bursts from repeater FRB20200120E are plotted in red crosses and the red circle. Bursts from FRB sources 121102 and 20180916B (labelled 180916 in the plot) are also easily identified. 190523, 190614, and ASKAP FRBs also represent observed FRBs. SGR1935+2154 radio bursts and plotted within the light grey region. They have frequency widths well within FRB ranges but below the FRB lower energy bound. With the new data from FRB20200120E, the galactic magnetar inches closer to being considered a true galactic FRB source.

Chapter 3

Breakthrough Listen Data of FRB121102

3.1 Breakthrough Listen Data

Breakthrough Listen is a project funded through the Search for Extraterrestrial Intelligence (SETI). One goal of SETI is to observe unknown radio sources in an attempt to discover any underlying transmission from extraterrestrial lifeforms. FRBs originate from unknown sources, making them a great candidate for SETI projects. The Breakthrough Listen observations of FRB121102 were conducted on August 26, 2017 during a 6 hour observation block [5]. The data were recorded with the 4-8 GHz (C-Band) receiver at the Robert C. Byrd Green Bank Observatory. During the first hour of observations, the telescope was calibrated and no data were recorded. All of the remaining hours were split into 30 minute intervals and numbered 11 through 20. Interestingly, 18 of the 21 bursts detected are in scan 11 and the remaining 3 are in scan 12. Scans 13-20 show no signal above the threshold detection S/N of 6. Bursts were named using the scan number followed by a letter, corresponding to their order of arrival. Bursts 11L, 11P, and 11R were not able to be flux calibrated during observations and are therefore not used in our analysis. Gajjar et al. [5] mention heavy radio frequency interference (RFI) below 4.5 GHz so the data from 4 GHz to 4.5 GHz were removed.

The burst snapshots contain all relevant observational information and are available for public download from the SETI data catalogue. These snapshots contain 20 milliseconds of high resolution data around the approximate TOA of the initial 21 bursts detected by Gajjar et al. [5]. The high resolution data have temporal and spectral resolutions of 10.1 μs and 183 kHz, respectively. Burst snapshot files are in archive format and can be opened with the Archive class in the PyPulse software package [34]. All of the files contain a 2 dimensional array of data. The 2D array is organized so that the first array is the lowest frequency channel and each consecutive array increases in frequency. These sub-arrays contain flux values which can be plotted versus time as a time-series. The entire frequency bandwidth of time-series are plotted together to obtain the full dynamic spectrum. Dynamic spectra are a commonly used method of visualizing radio data. All dynamic spectra are structured with the horizontal axis as time, the vertical axis as frequency, and the color as intensity.

Data plots of bursts 11A and 12B can be seen in figure 3.1. They are in the 2 dimensional, dynamic spectrum plot style just described. Real time values are not necessary for our analysis so our dynamic spectra begin at arbitrary 0 milliseconds along the horizontal axis. Most of the dynamic spectra in figure 3.1 is blue, which is background noise without any signal. Yellow streaks can be seen on the right side of the dynamic spectrum of 11A and left side of 12B. These streaks are the FRB.

After opening the data, we perform an automatic RFI search that finds wildly varying frequency channels and replaces their flux values with the average background noise level. We then apply an average in both the frequency and time directions. Averaging neighboring data bins improves signal visibility in dynamic spectra and increases computational efficiency. Our data initially contains 19,456 frequency channels and 2,048 time bins. A frequency averaging factor of 304 is applied, reducing the number of frequency channels down to 64. A time averaging factor of 4 is applied, reducing the number of time bins down to 512. The averaged temporal and spectral resolutions are 40.4 μs and 55.6 MHz, respectively. This is with the exception of burst 12B, which has 3,000 time bins. We average burst 12B by a factor of 6 in time, resulting in 500 time bins and a temporal resolution of 60.6 μs.

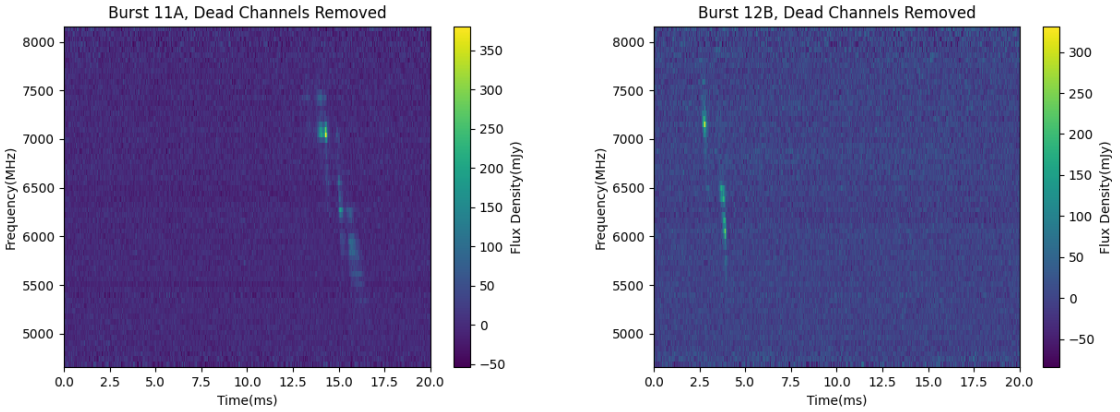

(a) Dynamic spectrum of burst 11A.

(b) Dynamic spectrum of burst 12B.

Figure 3.1: Dedispersed dynamic spectra of multicomponent FRBs. The horizontal axis is time, the vertical axis is frequency, and the color scale represents intensity. Bursts 11A and 12B are the two multicomponent bursts in the Breakthrough Listen data set. Dead channels, or those containing significant RFI, have been removed.

3.2 Power Law Spectrum

FRB spectra are well modeled by a power law with a high frequency turnover. Breakthrough Listen data demonstrate this property for all bursts [5]. The intensity is observed to increase from low frequency to high frequency as ν^{α}. α is the spectral index and is negative for all coherent emission processes. The intensity then decreases rapidly at the highest frequency end of the signal. A power law model indicates that our assumption of a compact object source is well founded. Compact object radio emissions exhibit power law spectra, whereas stellar sources have blackbody spectra. Our analysis builds on this idea with a more detailed measure of burst structure. This can then be used to constrain the source object even further.

3.3 Breakthrough Listen FRB Structure

Bursts 11A and 12B both show multicomponent structure. In figure 3.1, it can be seen that burst 11A has 4 components, and burst 12B has 2 components. There are many theoretical explanations for this multicomponent structure in FRBs which can be found within the FRB Theory Catalogue. No consensus has been made regarding the origin of multicomponent

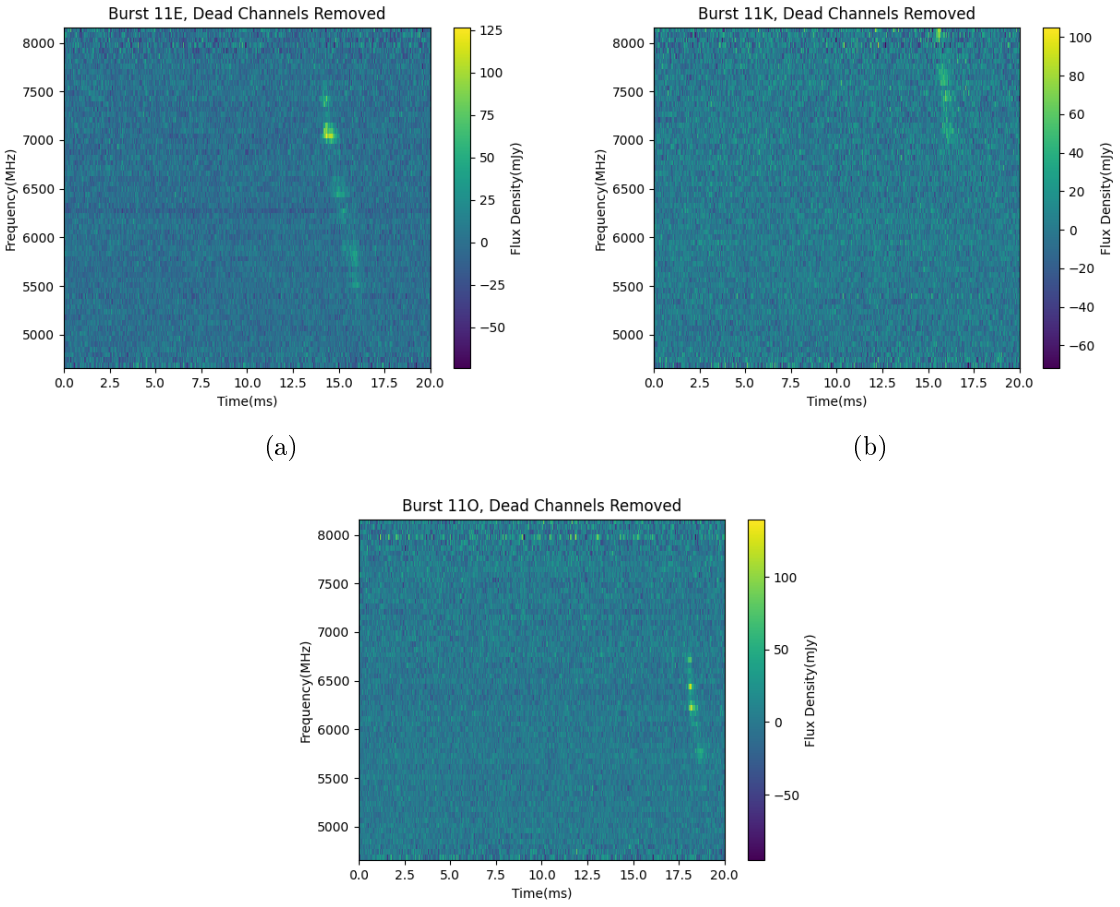

Figure 3.2: Dynamic spectra of unresolved multicomponent bursts.

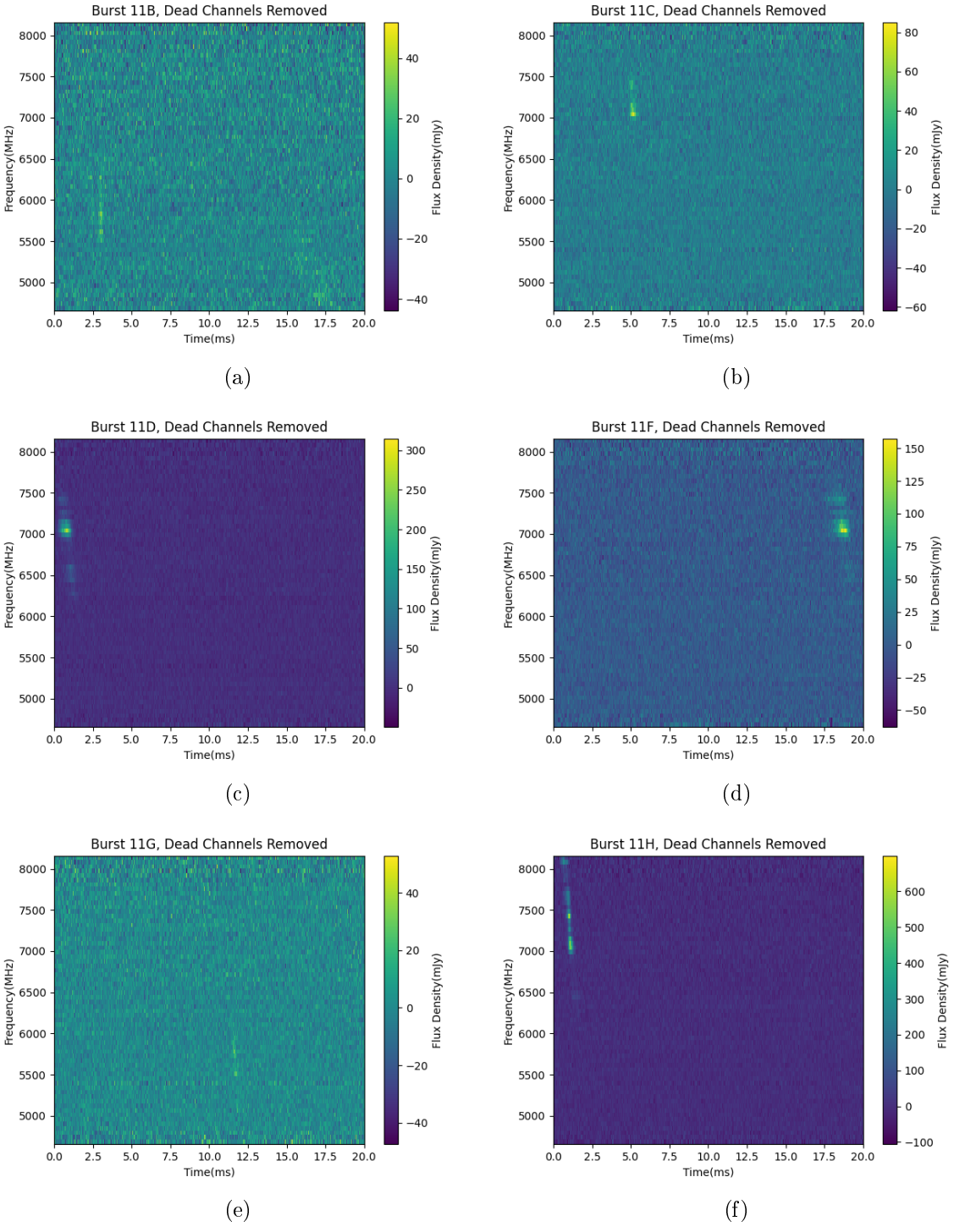

(a) (b) (c) (d) (e) (f)

Figure 3.3: Dynamic spectra of single component bursts.

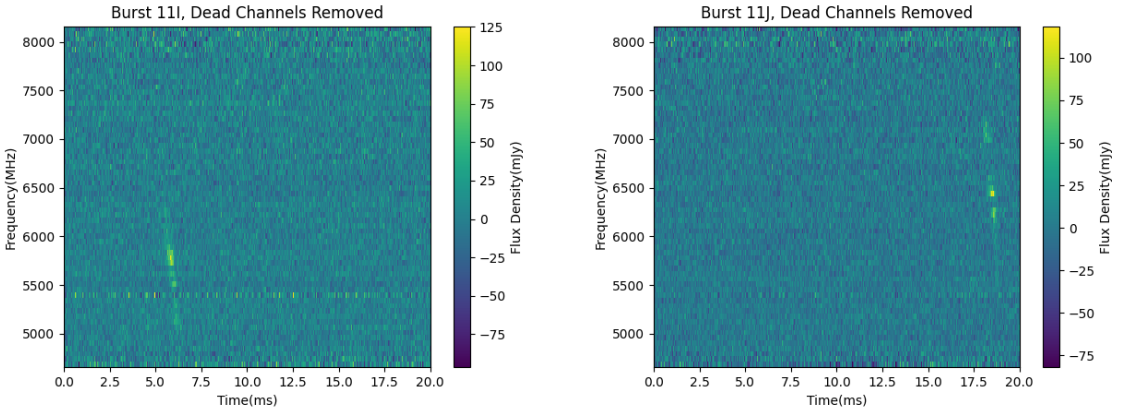

(a)

(b)

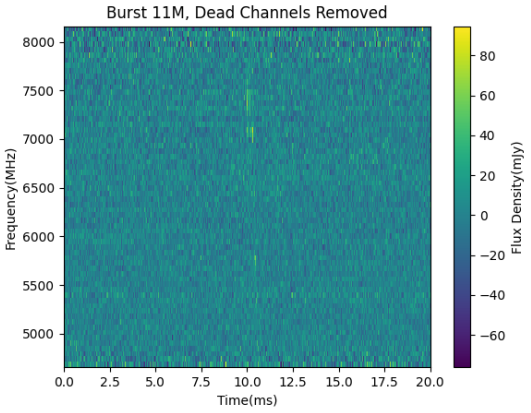

(c)

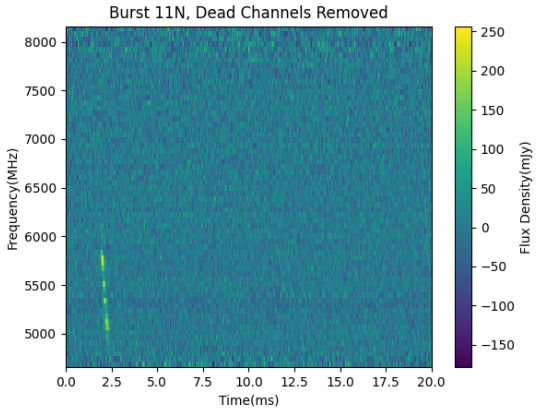

(d)

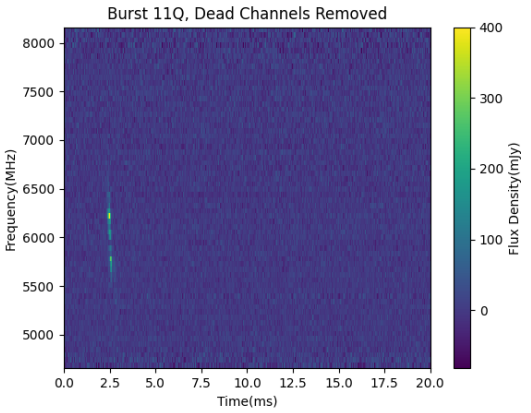

(e)

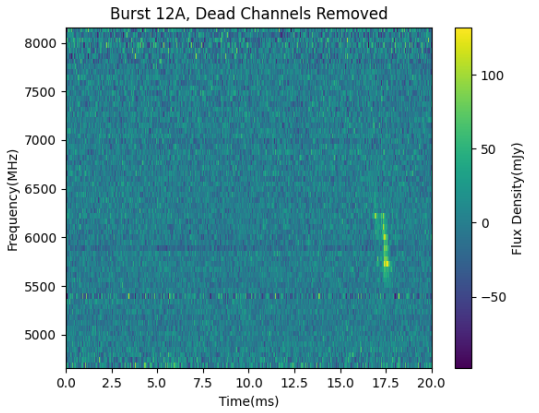

(f)

Figure 3.4: Dynamic spectra of single component bursts (continued).

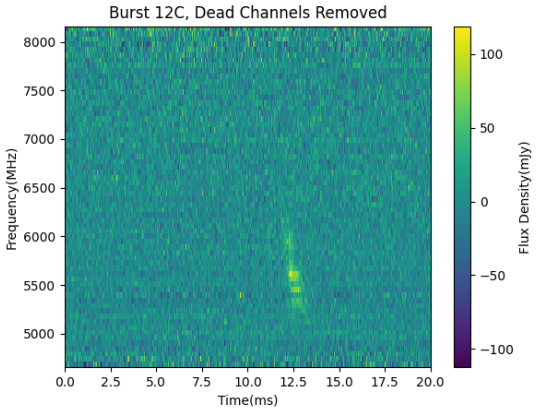

(a)

Figure 3.5: Dynamic spectra of single component bursts (continued).

structure as of the time of this writing. Both bursts 11A and 12B also show a "sad trombone" feature, which is common to repeater bursts. The sad trombone FRB feature is a downward marching of the signal in frequency over time. This nickanme was given to FRBs with this shape after the sad sounding musical tune a trombone makes when descending notes in equal intervals.

In addition to these bursts, Gajjar et al. [5] note that bursts 11E, 11K, and 11O show signs of multiple separate components. These bursts can be seen in figure 3.2. There are indeed breaks in the emission, but no emission with the same frequency both before and after the break. Because of this, it is impossible to be certain if the breaks are inherent to the emission mechanism or are a result of noise. Bursts 11(E,K,O) also have a downward-stepping slope resembling the sad trombone structure when dedispersed to their respective structure maximizing DM value. These bursts were designated unresolved multicomponent bursts because of the possibility of hidden components. However, without clear temporal breaks in the emission at the same frequency, they cannot be considered true multicomponent bursts.

Bursts 11D and 11F also show some slanting features which may be caused by hidden components. There is no indication of multiple components, however, so this idea is not investigated in our analysis. Bursts 11D and 11F dynamic spectra, as well as the remaining dynamic

spectra, can be seen in figures 3.3-3.5. With 2 FRBs clearly showing multiple components and many other FRBs showing signs of multiple components, the Breakthrough Listen data set is rich in its potential to learn more about FRB sources. We focus our research on understanding any differences between multiple and single component FRBs, if there are more components hidden in FRBs than those that can be seen over the noise level, and what emission process may cause these sepearate components.

3.4 Temporal Component Fitting

The first step in our analysis was to fit one or more curves to the burst data. We chose to fit a Gaussian curve to each burst at each frequency channel. An example of a Gaussian fit to a frequency channel of burst 11A is shown in figure 3.6. FRBs are assumed to be impulsive events, making a Gaussian fit physically accurate for modelling the data. Single component bursts are fit with a maximum of one component. The multicomponents bursts, 11A and 12B, are fit with four and two component maximums, respectively. The previously mentioned unresolved multicomponent bursts are fit with a maximum of one component for this stage of our analysis. We later explore the possibility of fitting them with multiple components.

Burst 11A has four components and in figure 3.6 it can be seen that there are three Gaussian curves fit at that particular frequency. However, many frequency channels have only one or zero components. PyPulse carries out the fit routine when given a maximum number of components. PyPulse's fitting routine determines the best fit using the least squares function. This function can be found in "optimize" within the scipy Python package. The PyPulse fitting routine can be found in "utils" and can fit any number of Gaussian components to time-series data. If the FRB is distinguishable above noise, it is fit with a Gaussian component. That component is then added to our model. If a component had previously been added to the model, it is refit in order to minimize the total model residual. This is done iteratively, until the maximum number of components is reached. If a frequency channel contains less components than the given maximum, like the time-series in figure 3.6, our fit function returns a Gaussian curve with zero amplitude (flat line).

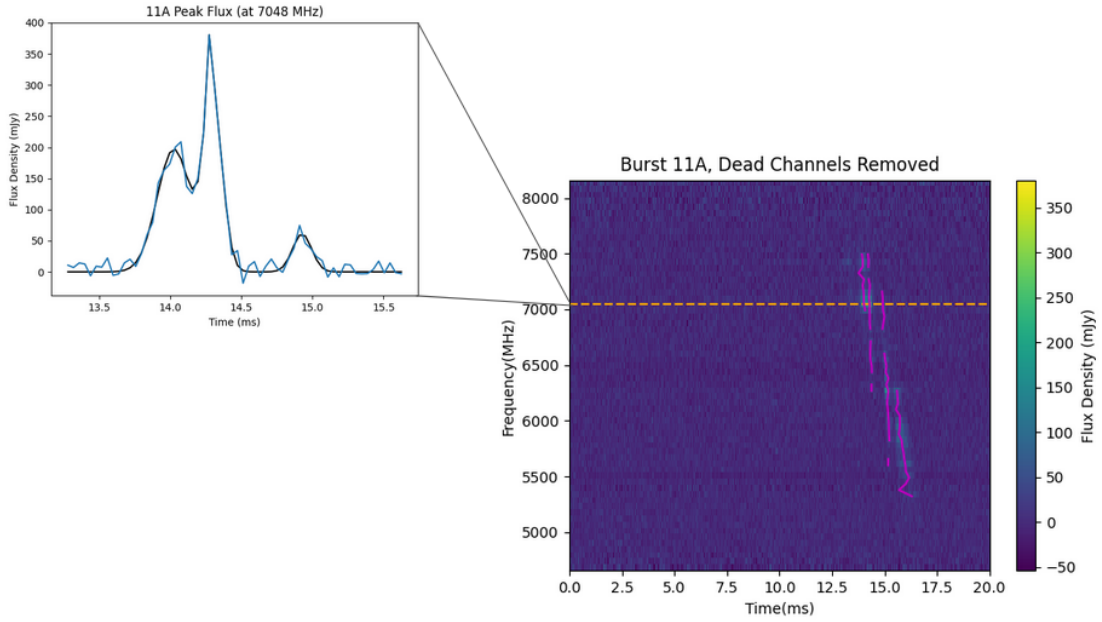

Figure 3.6: Model diagram of burst 11A. Right: The dynamic spectrum of burst 11A with the centers of each fitted Gaussian curve overlaid as magenta lines. Left: Time-series showing the fit of three separate Gaussian components to the signal at the frequency channel containing the maximum recorded flux value. The time-series is only plotted near the burst TOA for better visualization.

The best fit parameters are found for each burst component at each frequency channel. These parameters are the Gaussian center (mathematical mean, μ), width (mathematical standard deviation, σ), and amplitude, A. Any components with zero amplitude are ignored. The dynamic spectrum in figure 3.6 is a visualization of where the Gaussian fits are centered. The characteristic downward frequency drifting is clear to see with the model overlaid.

A source of error in this fitting process comes from frequency channels on the high and low frequency ends of each burst. The fitting routine returns nonzero fit parameters for some frequency channels which do not have any true signal. It is assumed that the fit routine attempts to fit a Gaussian curve to the largest noise spike, when given a frequency channel with only background noise. Each burst was inspected individually to find the high and low frequency limits of burst emission. These are entered as manual frequency cutoffs that stop the fitting routine outside of burst frequency ranges. These cutoffs extend beyond the frequency range (determined visually) of the signal by three frequency channels. This is to allow for

modelling of any signal which is too dim to see on dynamic spectra. The overestimation caused by this is included in our error.

Chapter 4

Fluence Moment Analysis

4.1 Measuring Burst Shape

Fluence is a good measure of a source's total energy output at a given frequency. It is commonly used when analyzing radio data. Using integration, time can be eliminated as a variable before proceeding in analysis. After obtaining a temporal fit for our set of FRBs, we integrated the fitted curves, resulting in a fluence value. This is done by simply summing the flux values obtained from each Gaussian curve. Flux density units are also converted to Janskys (from milliJanskys) in order to yield fluence in its standard form for FRB research (Jansky-milliseconds). Separate fluence values are calculated for each component of multicomponent bursts. We use our calculated fluence values to create a fluence distribution, a plot of fluence versus frequency. The fluence distribution for burst 11A can be seen in figure 4.1.

To test if multicomponent bursts are a distinct type of FRB, we compare their fluence distributions to those of the single component bursts. The most straightforward way of doing this is to compare the statistical moments of the two. Statistical moments are a mathematical method which can attribute a value to the shape of a distribution. The moments we calculate are standard deviation, skew, and kurtosis. The true second moment is variance, the square of standard deviation. Variance is less meaningful in the context of our analysis so we choose to compare standard deviation instead. An explanation is given following equation 4.1. We calculate fluence distribution moment values for each single component burst and each **com-**

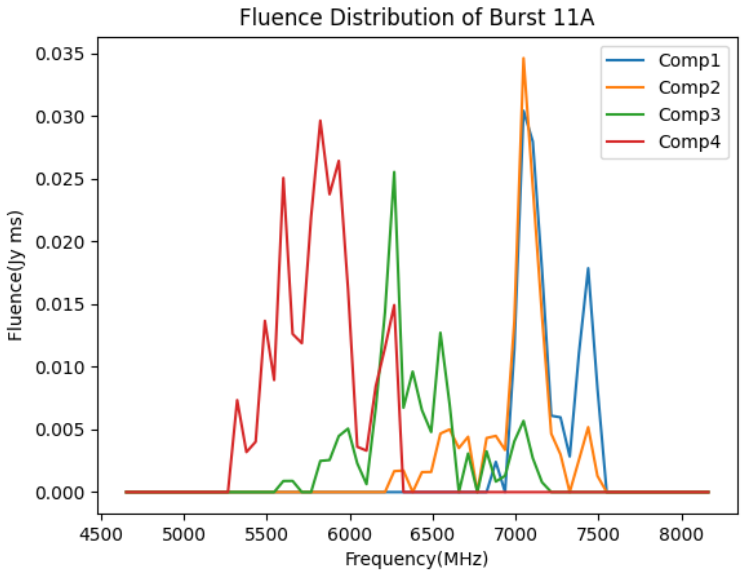

Figure 4.1: Fluence distribution of burst 11A. "Comp 1" - "Comp 4" in the legend refer to the components of the burst, ordered by TOA. Thus "Comp 1" refers to the bright, high frequency, leading component. Large fluctuations are reflective of uncertainty in our model. We attribute these fluctuations to fitting overestimation and distortion of burst shape by scintillation. A description of scintillation is given in chapter 5. Because we cannot properly quantify these errors, no error bars are given.

ponent of multicomponent bursts. Equations 4.1-4.3 give the numerical methods used to find moment values. In each equation, N represents the number of frequency channels and x_i represents the fluence of the i^{th} frequency channel.

$$\sigma = \sqrt{\frac{1}{N-1}\sum_{i=1}^{N}(x_i - \mu)^2} \tag{4.1}$$

Standard deviation is a measure of the fluence distribution spread. It essentially quantifies the width of the distribution in frequency. It is similar to the way the original Gaussian model quantified the width of the burst in time with its standard deviation. A large standard deviation implies that the components or bursts have a large bandwidth.

$$\tilde{\mu}^3 = \sum_{i=1}^{N}\left(\frac{x_i - \mu}{\sigma}\right)^3 \tag{4.2}$$

Skew indicates the presence of a "tail" in the distribution. Negative skew values indicate

that the components or bursts have a tail extended towards lower frequencies. Positive skew is the opposite, indicating a tail towards higher frequencies. A skew value of zero is only given to distributions which are perfectly symmetric about their mean frequency.

$$\tilde{\mu}^4 = \left[\sum_{i=1}^{N}\left(\frac{x_i - \mu}{\sigma}\right)^4\right] - 3 \tag{4.3}$$

Kurtosis is the statistical measure of peak strength. A kurtosis value of 0 is given to the normal distribution. Using this as a standardization, we calculate the excess kurtosis of single component bursts and the excess kurtosis of components within multicomponent bursts. An excess kurtosis of -1.2 describes a uniform distribution, whereas an excess kurtosis of 3 represents a Laplace distribution (exponential rise and fall).

Figure 4.2 shows the total fluence of each component/burst versus their respective fluence distribution moments. The components of both multicomponent bursts appear to be in the same range of values as single component bursts. We note that burst 11A has a wide range of values for both skew and kurtosis. Burst 12B also has a large range in kurtosis values for its components. Because the size of our data set is small (< 30), we cannot perform statistical measures to decide if the multicomponent moments are different than the single component moments. This may be possible with a larger data set. It can be argued that the multicomponent bursts appear to take the same moment values as single component bursts. This may point towards both types of bursts originating in a similar manner. We next present some methods used to support this claim.

4.2 Burst 11A and 12B S/N Reduction

An insightful experiment is to reduce the S/N of both multicomponent bursts and repeat the previous analysis. Burst 11A has an original S/N of 36.8 and burst 12B has an original S/N of 21.7. Both of these values are much greater than the average S/N of the Breakthrough Listen data set. We calculate the average value to be 13.3 using an unweighted average. This raises the question: Do single component bursts have a hidden multicomponent structure

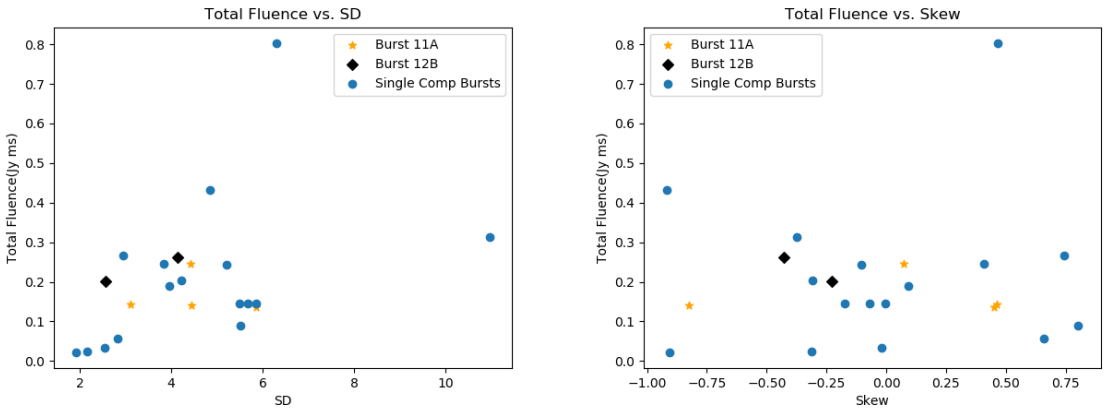

(a)

(b)

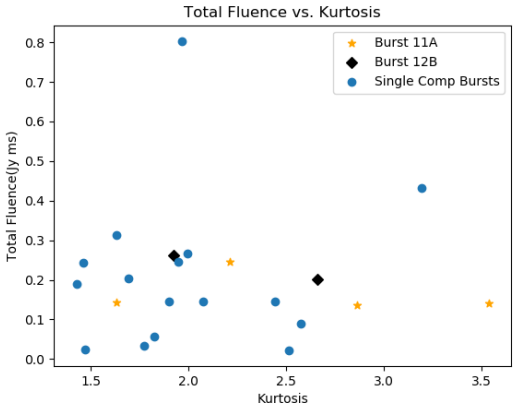

(c)

Figure 4.2: Fluence distribution moments.

that has been "washed out" by noise? Given the large distance to FRB sources, it is likely that interference could decay parts of the emission until they are indistinguishable from noise. The presence of so-called unresolved multicomponent bursts serves as a testament to this hypothesis.

Noise is added to the multicomponent bursts in order to reduce their S/N to a value near the data set average. The added noise is proportional to a ratio of the data set average S/N to the burst S/N. At each point in the data, the difference between the flux value of the point and the burst peak flux value is found. Added noise is proportional to this difference as well. Finally, we multiplied the added noise by a random number between 0 and 1 which mimics the random deviations of background noise. After this process, burst 11A has a new S/N of $\sim$17 and burst 12B has a new S/N of $\sim$10. Another outcome of this process is the "loss" of one component in both multicomponent bursts. This is decided by our fit routine, which yeilds three and one separate components for burst 11A and 12B, respectively. In our fit, the leading component of burst 11A merges with the second component and the components of burst 12B are no longer clearly separated.

It can be seen in figure 4.3 that, when the S/N of the multicomponent bursts is decreased, the large range in skew and kurtosis values of burst 11A become much smaller. This may indicate a trend towards less extreme values of these moments for bursts with lower S/N. However burst 12B does not show this effect. Its single detected component has opposite sign, but similar magnitude, skew as one of the initial components. The kurtosis is also nearly the same as one of the initial components. The standard deviation of burst 11A components do not appear to change significantly. Burst 12B standard deviation does increase, but this can easily be explained by components merging. The two original components of burst 12B occupy very different frequency ranges, giving the fluence distribution a large width when the entire burst is fit as one component. We choose not to explore changes in standard deviation any further.

We next decrease the S/N of the multicomponent bursts until burst 11A has only one detectable component. Results for this step are shown in figure 4.4. The S/N of burst 12B

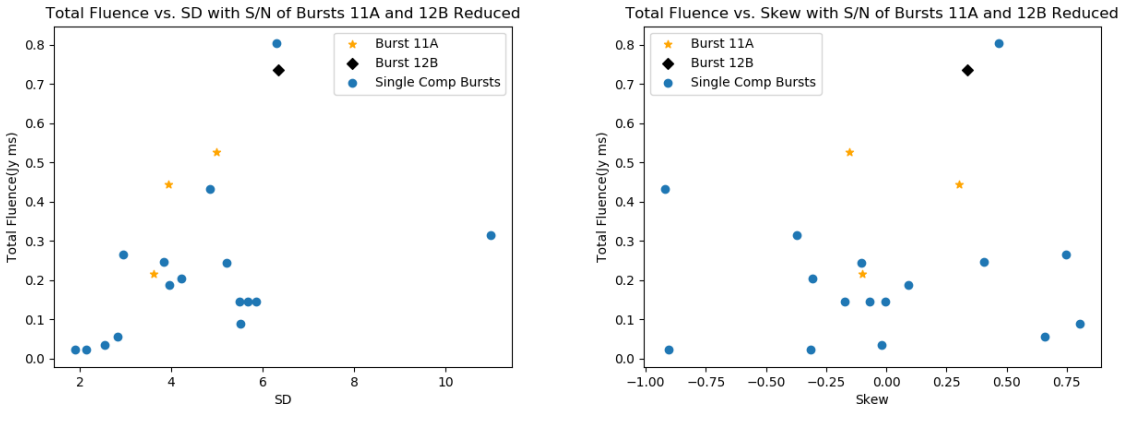

(a)

(b)

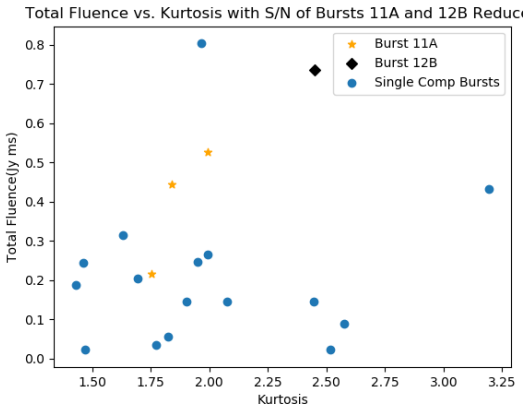

(c)

Figure 4.3: Fluence distribution moments with the S/N of bursts 11A and 12B decreased to near average values.

is reduced further to observe the effect a S/N reduction has on artificially unresolved multicomponent bursts. In this case, the skew of burst 11A becomes a similar value to one of its previous components. The same effect is observed for burst 11A kurtosis. This may be due to the brightest component dominating the burst signal at very low S/N. Burst 12B skew becomes only slightly larger, however its kurtosis decreases dramatically, which is likely due to the bright peak becoming shrouded in noise.

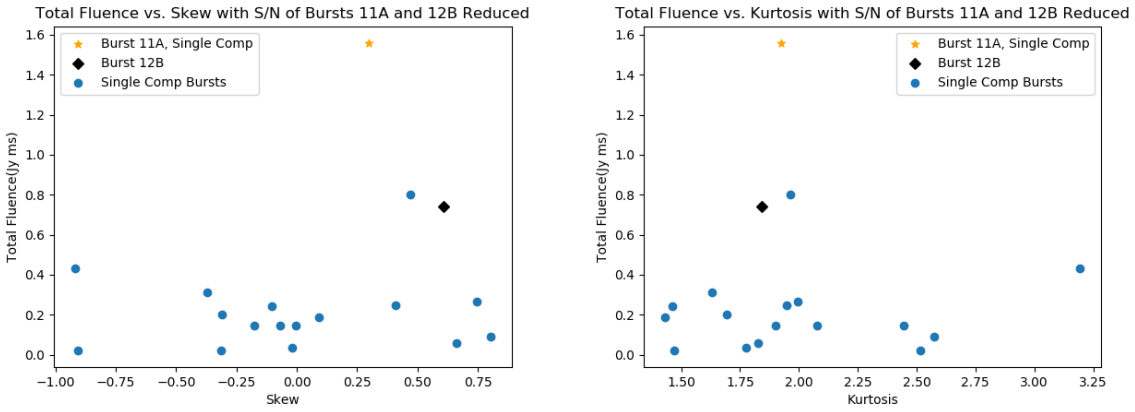

(a) (b)

Figure 4.4: Fluence distribution moments with the S/N of bursts 11A and 12B decreased until burst 11A has only 1 detectable component.

4.3 Kolmogorov-Smirnov Analysis

A Two-Sample Kolmogorov-Smirnov (KS) test is a common statistical method used for determining the similarity of two empirical cumulative distribution functions (ECDF). We perform a KS test on the moment values of both single component bursts and the components of multicomponent bursts. The assumed null hypothesis is: "the moments of bursts and individual components are taken from the same distribution". If the maximum difference between the ECDFs of single and multicomponent burst moments is greater than the KS criterion, the null hypothesis is rejected. The KS test criterion is given by equation 4.4.

$$D_{n,m} > \sqrt{-\ln\left(\frac{\alpha}{2}\right)\frac{1+\frac{m}{n}}{2m}} \tag{4.4}$$

We take m as the number of components in multicomponent bursts and n as the number of single component bursts. In this equation, α is the alternative hypothesis probability and $D_{n,m}$ is the maximum difference between the ECDFs. The alternative hypothesis probability is the likelihood that our null hypothesis is incorrect. In our KS test analysis, we include the unresolved multicomponent bursts with the multicomponent burst (m) sample. To do this, we fit the unresolved multicomponent bursts with two components and a manually entered separation in the signal. This separation is chosen by eye to match the temporal location of the expected break in emission. Previously calculated unresolved multicomponent burst moments are used in the single component (n) sample as well. We use unresolved multicomponent bursts in both samples. This creates similar size samples, with 12 separate components in our m sample and 16 bursts in our n sample.

The maximum difference between the ECDFs is calculated for standard deviation, skew, and kurtosis. These differences are then used to invert equation 4.4 and solve for the α inequality. The α inequality will provide a maximum likelihood that the samples come from different distributions. We find that this test only rejects the standard deviation at a $\alpha \leq 0.64$ level. This can be interpreted as a maximum 64% probability that the standard deviation of the two sets come from the different distributions. The values of α for skew and kurtosis are $\alpha \leq 1.50$ and $\alpha \leq 1.23$, respectively. These values are not statistically meaningful because α cannot be greater than one. Therefore they cannot be interpreted in our analysis.

4.4 Extended Data Set

The initial search for FRBs during the Breakthrough Listen observations found 21 bursts above the signal to noise search threshold of 6. A later analysis of the data set used a much lower signal to noise threshold of 3 and a machine learning approach in an attempt to find fainter bursts missed by the original scan [8]. This search claims to have discovered an additional 72

bursts existing in the filterbank data. We perform a search of the filterbank data in an attempt to find these bursts. Our fit routine could only fit 32 of the 72 low S/N bursts, when given a 20 ms region centered on the TOA listed in Zhang et al. [8] to search. The filterbank data originally contains 10912 frequency channels, which we average by a factor of 682, resulting in 16 frequency channels. Very low resolution is necessary to average down noise relative to the FRB. Once fit, we put the new set of bursts through the same analysis as the original set. The moment scatterplot containing the 50 total bursts can be seen in figure 4.5.

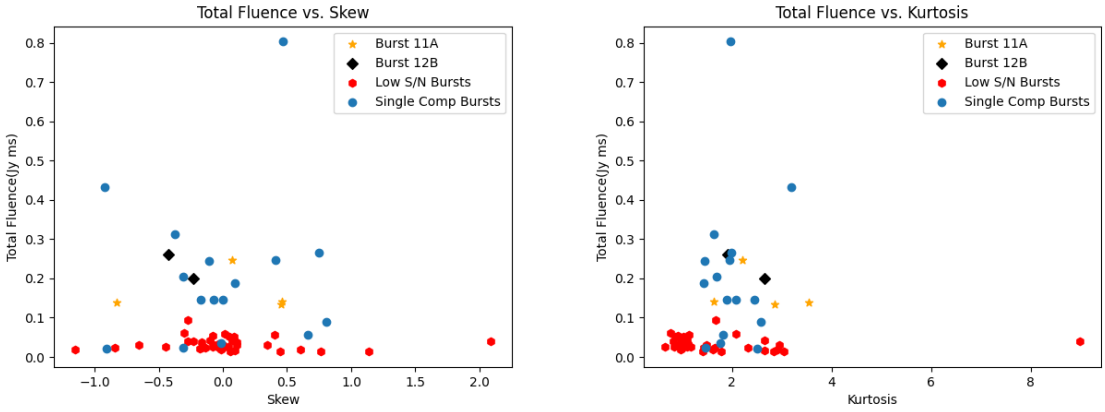

(a) (b)

Figure 4.5: Fluence distribution moments of the bursts listed in Zhang et al. [8] are plotted in red. We were only able to find 32 bursts in this data set, likely due to differences between our fitting method and the machine learning method.

Most of the new bursts appear to inhabit the same range of moment values as the original set of bursts. However, the low resolution needed to identify the new bursts could bias their moment values. Most of the bursts only occupy a few frequency channels. A clear example of this bias can be seen in both subplots of figure 4.5. There is an extreme outlier with a kurtosis value of $\sim$9 and skew value of $\sim$2. This is an incorrect value because the burst only occupies one frequency channel. Because of the unreliable statistical measures, we choose not to interpret the extra bursts in our analysis any further.

Chapter 5

Breakthrough Listen Scattering Analysis

5.1 What Is Scattering?

All radio observations are affected by scattering in some way. Scattering, like dispersion, is caused by the ISM and IGM. When radio waves travel through these media, their raypaths are distorted. This distortion makes some raypaths slightly longer than the direct line from the source to the observer. Figure 5.1 illustrates this idea. Because some raypaths are longer than others, those parts of the signal will take longer to arrive. The resulting signal we observe is a broadened pulse, with an emission tail immediately following the TOA.

The distortion of the signal is commonly modelled as a Gaussian curve convolved with an exponential decay as can be seen in figure 5.2. The Gaussian is the assumed shape of the signal, whereas the exponential decay is the extended scattering tail. If not accounted for, the exponential decay will cause an FRB to seem longer in duration than it truly is.

Scattering can also focus the waves like a lens, making them appear as bright patches in dynamic spectra. These bright patches are known as "scintles" to radio astronomers. An example of radio data with clearly visible scintles can be seen in figure 5.3. While spurious scintles and scatter broadening are not visible in the dynamic spectra of Breakthrough Listen

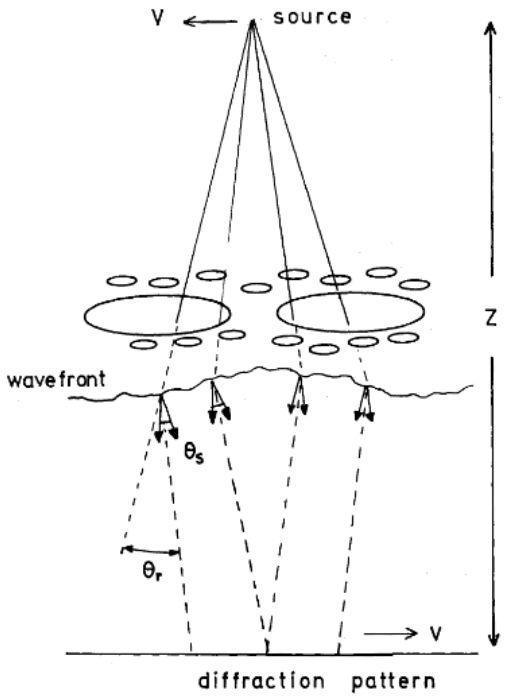

Figure 5.1: Raypath distortion from an intervening scattering medium (figure 1, Hewish [9]). Ovals between the source and observer represent this medium. Raypaths are distorted by a small angle labeled θ_s. Many diffracted rays emerge from the medium and become the distorted wavefront. There will also be some relative velocity, v, of the source relative to the observer. The result is the observer seeing the distorted wavefront as a moving diffraction pattern (scintles in a dynamic spectrum). It is clear that some raypaths are longer than others, thus the signal will be scatter broadened.

data, scattering may have an effect on our analysis. If the signal has been distorted into a significantly non-Gaussian shape in time, it could lead to calculated statistical moments values which are not intrinsic to the source. We use statistical moments to quantitatively describe burst shape in our analysis. Therefore, any scattering induced distortion to burst shape should be investigated rigorously.

5.2 Scattering Timescale

The scattering timescale is the average temporal broadening of a signal. A larger scattering timescale indicates that signals are longer duration due to scattering. Scattering timescales are

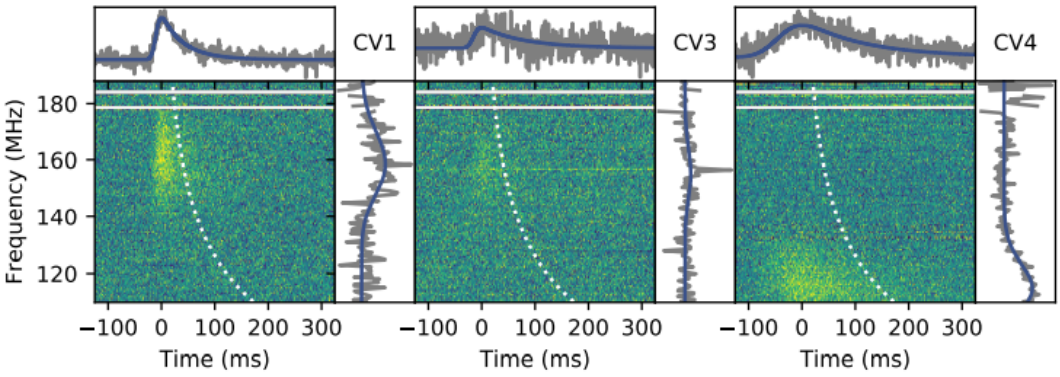

Figure 5.2: Dynamic spectrum from an observation of FRB20180916B (figure 3, Pleunis et al. [10]). The band-averaged time series at the top panel of each burst shows the large emission tails of these FRBs. The blue line in the time series is a Gaussian curve convolved with an exponential decay. This is the model used to represent the scattered signal. The dotted white line is the expected scattering tail as a function of frequency. Note that this is not an effect of dispersion.

an extremely useful way to measure how much of an impact scattering has on analysis of radio data. If the scattering timescale is much smaller than the signal time length, then scattering does not significantly affect the analysis. FRBs from the 121102 source are on the order of a millisecond in duration. Because broadening is not qualitatively seen in the Breakthrough Listen data, the scattering timescale must be less than a millisecond. Breakthrough Listen data contains no clearly observed scatter broadening, making an accurate measurement of the scattering timescale using the data impossible.

The equation which describes the scattering timescale is given by equation 5.1. It is dependent on the speed of light (c), the distance to the source (D), and the mean-square scattering angle per unit distance (η) [35]. Both the speed of light and the distance to FRB121102 have well known values of $3 \times 10^8 \frac{\mathrm{m}}{\mathrm{s}}$ and 972 Mpc, respectively. η is itself dependent on multiple other variables and will be discussed later on. We first use the scattering timescale equation to estimate the effect scattering has on this analysis.

$$\tau_d = \frac{\eta_0 D^2}{12c} \tag{5.1}$$

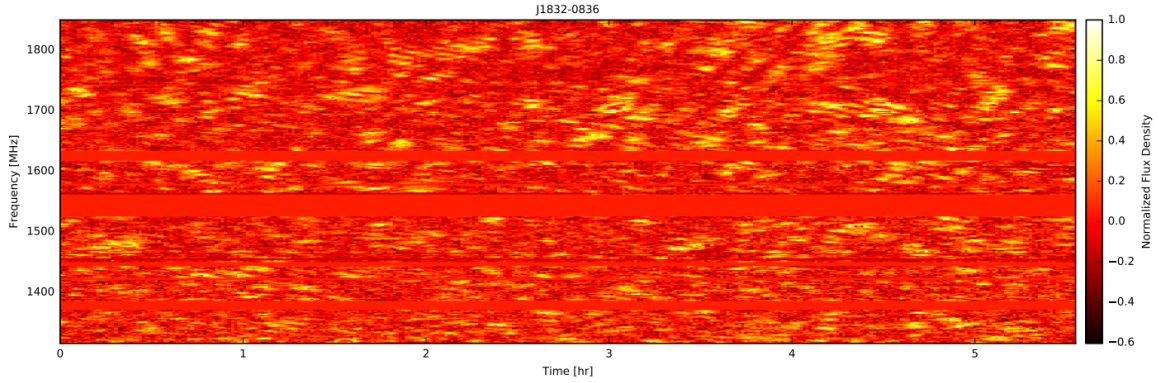

Figure 5.3: Dynamic spectrum from an observation of pulsar J1832-0836. Many scintles can be seen as bright, high intensity areas throughout the plot. (Adapted from figure 1, Shapiro-Albert et al. [11])

Scattering timescales can be theoretically determined for sources in the Milky Way using the NE2001 survey [3]. From this survey, Gajjar et al. [5] estimate a Milky Way contribution to the scattering timescale of $\tau_d = 20\nu^{-\alpha}\mu$s where $4 \leq \alpha \leq 4.4$. For the 4-8 GHz range of the Breakthrough Listen data, this corresponds to a maximum scattering timescale of 78 nanoseconds at the bottom of the frequency band and just 5 nanoseconds at the top of the band. Scattering timescales are much more difficult to determine for the IGM. This is because of the wide range of values η might take in the IGM. FRB121102 is an extragalactic source, making an accurate IGM scattering timescale contribution impossible to determine with current theory. However, with use of some approximations, a range of values can be solved for. This range will determine the magnitude which our analysis is affected.

Another form of the scattering timescale equation is inversely proportional to the frequency bandwidth of the FRB and is given by equation 5.2 [35]. The constant C_1 is of order unity, but can vary based on the geometry of the medium. This equation is only used as an approximation because FRB bandwidths can vary significantly. Assuming a frequency width of roughly 1 GHz, the scattering timescale will be $\frac{1}{2\pi}$ nanoseconds in length. If this approximation lies within our derived range, we will have good evidence for small scattering timescales.

$$\tau_d \sim \frac{C_1}{2\pi\Delta\nu} \tag{5.2}$$

5.3 IGM Turbulence Parameter Values

As mentioned previously, η is dependent on multiple other variables. η can be generally described as a measure of the turbulence of the medium which observed radio signals travel through. The η_0 variable in equation 5.1 is the value used for sources observed in the Milky Way. This value is approximately 3.2 $\text{mas}^2\,\text{kpc}^{-1}$ but can vary significantly depending on the line of sight. This also changes for sources outside of our galaxy because η itself relies on multiple variables which have unknown IGM values. Equation 5.3 is used to find the value of η [11].

$$\eta_0 \approx 3.2\,\text{mas}^2\,\text{kpc}^{-1}\left(\frac{\nu}{1\text{GHz}}\right)^{-4}\left(\frac{l_1}{100\text{km}}\right)^{-1/3}\left(\frac{C_N^2}{10^{-3.5}\text{m}^{-20/3}}\right) \tag{5.3}$$

From equation 5.3, it can be seen that η relies on the frequency of observations (ν), the inner scale (l_1), and the electron-density wavenumber spectrum amplitude (C_N^2). The frequency of Breakthrough Listen observations of FRB121102 are in the range of $4\text{GHz} \leq \nu \leq 8\text{GHz}$. Inner scale and wavenumber spectrum amplitude values are unknown outside of the Milky Way.

The inner scale represents the distance at which energy dissipates into a medium. It is inversely proportional to the upper wavenumber cutoff of the electron density wavenumber spectrum [35]. Inner scale values are distances at which motion within the medium is mostly dominated by thermal noise. It is related to the outer scale variable, which represents the longest "mixing" distance of the IGM. This mixing distance is the largest scale of energy injection from an object. The largest outer scale value of the IGM is theorized to be the distance which AGN jets travel before dissipating all of their energy [36]. Finally, the electron-density wavenumber spectrum amplitude is a measure of the turbulence's strength at a given length scale. A larger amplitude will make for a stronger turbulence.

An analysis of the values that C_N^2 may take for the IGM is carried out by Macquart et al. [36]. In their analysis, they present an equation which can determine the wavenumber spectrum amplitude of an intergalactic source using its redshift. Equation 5.4, combined with the likely range of outer scale (L_0) values given by Macquart et al [36], is used to find a range

Symbol	Definition	Units
τ_d	Scattering Timescale	s
c	Speed of Light	$\frac{\text{m}}{\text{s}}$
D	Distance to Source	Mpc
η	Mean-Square Scattering Angle per Unit Distance	$\text{mas}^2\text{kpc}^{-1}$
η_0	Mean-Square Scattering Angle per Unit Distance, Nominal Milky Way Value	$\text{mas}^2\text{kpc}^{-1}$
ν	Observation Frequency	GHz
C_1	Constant in Uncertainty Relation	1
l_1	Inner Scale	km
L_0	Outer Scale	pc
C_N^2	Electron-Density Wavenumber Spectrum Amplitude	$\text{m}^{-20/3}$
z	Source Redshift	1
Ω_b	Cosmic Baryon Density	1
f	Constant of Order Unity	1
α	Spectral Index	1
v	Relative Velocity	$\frac{\text{m}}{\text{s}}$
θ_s	Scattering Angle	rad
θ_r	Angular Deflection	rad

Table 5.1: Scattering variables

of wavenumber spectrum amplitude values for FRB121102.

$$C_N^2 = 9.42 \times 10^{-14}(1+z)^6 f^2 \left(\frac{\Omega_b}{0.04}\right)\left(\frac{L_0}{1\text{pc}}\right)^{-2/3} \text{m}^{-20/3} \tag{5.4}$$

Equation 5.4 is dependent on the redsift of the source, z, a constant, f, the cosmic baryon density, Ω_b, and the outer scale, L_0. The redshift of FRB121102's host galaxy is 0.19273, f is of order unity and assumed to be 1, and the cosmic baryon density we assume to be 0.04.

While the exact value of the wavenumber spectrum amplitude, C_N^2, is unknown for the IGM, a range of outer scale values can be used to find the possible wavenumber spectrum amplitude values. Macquart et al. [36] give a generous range of outer scale values $0.001\,\text{pc} \leq L_0 \leq 0.1\,\text{Mpc}$. We first used this range of outer scale values to solve for the plausible range of C_N^2 using equation 5.4. This yields a range of $1.26\times10^{-16}\,\text{m}^{-20/3} \leq C_N^2 \leq 2.71\times10^{-11}\,\text{m}^{-20/3}$. From equations 5.1 and 5.3, we find that the scattering timescale is directly proportional to η_0 which is in turn directly proportional to C_N^2. Our last step is to use those equations to determine an upper limit for the scattering timescale.

5.4 Conclusions on Scattering

We assume an inner scale value of 100 km, the value commonly used to estimate the Milky Way scattering timescale, as given by Cordes and Rickett [35]. The inner scale distance could be much larger within the IGM but this is only speculative. However, any larger values will decrease η_0, thus decreasing our theoretical upper limit on τ_d. The upper limit derived is $\tau_d \leq 0.21\,\mathrm{ns}$, which is nearly 7 orders of magnitude shorter in duration than the average FRB. This is also slightly larger than our previously determined approximation of the scattering timescale.

The largest contribution to scattering appears to come from the Milky Way. This may not be too surprising if the intervening IGM is assumed to be less turbulent than the local ISM. However, the Milky Way contribution is also very small. Totaling only 78 ns at the extreme lower end of the data frequency band. This maximum amount of scattering is 5 orders of magnitude less than FRB durations. We conclude that scattering does not have a significant effect on our results.

Another interesting unknown to investigate is the IGM inner scale value along the line of sight to FRB121102. Taking a scattering timescale of 1 nanosecond and our known range of C_N^2, we can determine this. It is acceptable to use a scattering timescale greater than our upper limit for FRB121102 because an increase to the inner scale decreases the scattering timescale. This means we are solving for a conservative lower limit of the true IGM inner scale value. figure 5.4 shows how the inner scale varies as a function of C_N^2, while τ_d is fixed. From the plot, we note that the inner scale can take a very wide range of values, much like the outer scale. We conclude that it is likely within the range $10^4\,\mathrm{km} \leq l_1 \leq 10^{16}\,\mathrm{km}$.

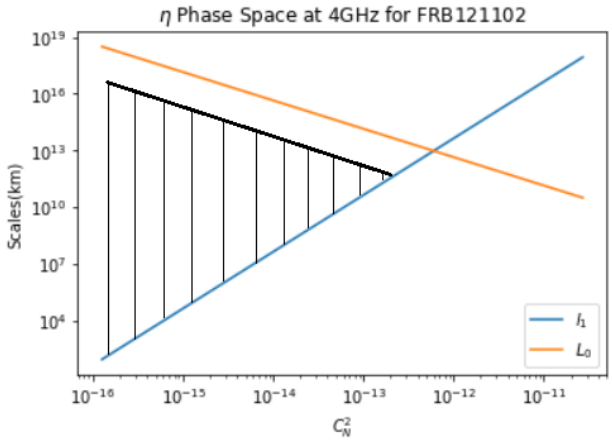

Figure 5.4: Phase space showing how the inner scale changes with $\tau_d = 1$ ns. The orange line indicates the outer scale values which are used to determine the wavenumber spectrum amplitude on the horizontal axis. The blue line represents the inner scale values derived from equation 5.3. Increasing the inner scale value decreases the scattering timescale. The actual IGM inner scale along the line of sight to FRB121102 must be above the blue line and well below the orange line. This region is shown by the vertical black lines.

Chapter 6

Conclusions and Future Work

6.1 Conclusions

Our analysis has provided a unique method for analyzing FRBs. The moment analysis carried out here can be used to compare multicomponent bursts to their single component counterparts. Separate components of multicomponent bursts extend across a wide range of both skew and kurtosis values. This range is also inhabited by single component bursts, indicating a similar emission process for both burst types. After reducing the S/N of multicomponent bursts to the data set average, the range of skew and kurtosis values decrease significantly for burst 11A. The multicomponent burst moment values appear to be closer to the average of the single component burst moment values after S/N reduction. This may suggest that some single component FRBs actually have multiple components which are not resolved due to noise. A larger proportion of multicomponent bursts would confirm or deny this hypothesis and further constrain the emission region of FRBs.

We also investigate the effect of scattering on the Breakthrough Listen data set. This is among the first analysis of extragalactic scattering along the line of sight to an FRB source. We find that scattering does not affect our results significantly. Our extragalactic scattering analysis also provides a constraint of the inner scale in the direction of FRB121102.

6.2 Future Work

In addition to bursts 11A and 12B, three bursts in the Breakthrough Listen data set showed unresolved multicomponent structure. Another two burst show indications of a downward frequency drifting structure. The unresolved multicomponent bursts show the frequency drifting common to multicomponent bursts, but do not have clear temporal separation between emission at the same frequency. The lack of clear components may be an outcome of too weak S/N for separate components to be resolved properly. We attempt to investigate this with our KS test, but receive meaningless results with this data set. A deeper investigation into the question of whether unresolved multicomponent bursts do truly contain multiple components would be a valuable next step to our analysis. Moment values could be calculated for the manually separated, unresolved multicomponent bursts used in the KS test. Those moment values could then be added to figure 4.2 as supposed individual components.

There are many avenues of experimentation possible in our moment analysis. A comparison of the extended data set to the reduced S/N multicomponent bursts could lead to greater insight about burst shape. Including the extended data in the KS test may lead to statistically meaningful results. We caution that analyzing the extended data set should be done with a different fitting method, at a greater resolution. This will help avoid obtaining inaccurate moment values.

The final, and possibly most crucial future direction for our analysis, is to carry it out with multiple FRB sources. The methods demonstrated here can be applied to nearly any data. Our results from this data set will undoubtedly be biased by the fact that all of the bursts originated from the same source, within the same hour. We urge others to apply this method to as large an FRB data set as possible. It may be a key component to unveiling the mystery of FRBs.

Bibliography

[1] Lorimer D. R.; Bailes M.; McLaughlin M. A. et al. A Bright Millisecond Radio Burst of Extragalactic Origin. *Science*, 318:777, 2007. (document), 1.1, 1.1, 1.3

[2] Pleunis Z. http://frb2020.phys.wvu.edu/program.html. *FRB2020*, 2020. (document), 1.1, 1.2, 1.2

[3] Cordes J. M.; Lazio T. J. W. NE2001.I. A New Model for the Galactic Distribution of Free Electrons and its Fluctuations. *ePrint*, 2002. (document), 1.2, 5.2

[4] Marcote B.; Paragi Z.; Hessels J.W.T et al. The Repeating Fast Radio Burst FRB 121102 as Seen on Milliarcsecond Angular Scales. *ApJL*, 834:9, 2017. (document), 1.3, 1.3

[5] Gajjar V.; Siemion A.; MacMahon D. et al. Highest Frequency Detection of FRB 121102 at 4-8 GHz Using the Breakthrough Listen Digital Backend at the Green Bank Telescope. *RNAAS*, 231, 2018. (document), 1.4, 1.5, 3.1, 3.2, 3.3, 5.2

[6] Rajabi F.; Chamma M.A.; Wyenberg C.M. et al. A Simple Relationship for the Spectro-Temporal Structure of Bursts From FRB 121102. *MNRAS*, 498:4936–4942, 2020. (document), 2.1, 2.1

[7] Majid W. A.; Pearlman A. B.; Prince T. A. et al. A Bright Fast Radio Burst from FRB 20200120E with Sub-100-Nanosecond Structure. *ePrint*, 2021. (document), 2.2

[8] Zhang Y. G.; Gajjar V.; Foster G. et al. Fast Radio Burst 121102 Pulse Detection and Periodicity: A Machine Learning Approach. *ApJ*, 866, 2018. (document), 4.4, 4.5

[9] Hewish A. Frequency-Time Structure of Pulsar Scintillation. *MNRAS*, 192:799–804, 1980. (document), 5.1

[10] Pleunis Z.; Michilli D.; Bassa C. G. et al. LOFAR Detection of 110-188 MHz Emission and Frequency-Dependent Activity from FRB 20180916B. *APJ*, 911:18, 2021. (document), 1.2, 5.2

[11] Shapiro-Albert B. J.; McLaughlin M. A.; Lam M. T. et al. Analysis of Multi-hour Continuous Observations of Seven Millisecond Pulsars. *ApJ*, 890:18, 2020. (document), 5.3, 5.3

[12] Niu C. H.; Li D.; Luo R. et al. CRAFTS for Fast Radio Bursts: Extending the Dispersion-Fluence Relation with New FRBs Detected by FAST. *ApJL*, 909:7, 2021. 1.1

[13] Petroff E. https://www.frbcat.org/. *FRBCAT*, 2016. 1.1

[14] Chawla P.; Andersen B. C.; Bhardwaj M. et al. Detection of Repeating FRB 180916.J0158+65 Down to Frequencies of 300 MHz. *ApJ*, 896:13, 2020. 1.2

[15] Pilia M.; Burgay M.; Possenti A. et al. The Lowest Frequency Fast Radio Bursts: Sardinia Radio Telescope Detection of the Periodic FRB 180916 at 328 MHz. *ApJL*, 896:11, 2020. 1.2

[16] Gajjar V.; Siemion A.; MacMahon D. et al. Highest Frequency Detection of FRB 121102 at 4-8 GHz Using the Breakthrough Listen Digital Backend at the Green Bank Telescope. *ATel*, 10675, 2017. 1.2

[17] Chatterjee S.; Law C.J.; Wharton R.S. et al. A Direct Localization of a Fast Radio Burst and its Host. *Nature*, 541:58–61, 2017. 1.2, 1.3

[18] The CHIME/FRB Collaboration. Periodic Activity from a Fast Radio Burst Source. *Nature*, 582:351–355, 2020. 1.2

[19] Rajwade K.M.; Mickaliger M.B.; Stappers B.W. et al. Possible Periodic Activity in the Repeating FRB 121102. *MNRAS*, 495:3551–3558, 2020. 1.2

[20] Spitler L. G.; Cordes J. M.; Hessels J. W. T. et al. Fast Radio Burst Discovered in the Arecibo Pulsar ALFA Survey. *ApJ*, 790:9, 2014. 1.3

[21] Tendulkar S. P.; Bassa C. G.; Cordes J. M. et al. The Host Galaxy and Redshift of the Repeating Fast Radio Burst FRB 121102. *ApJL*, 834:8, 2017. 1.3

[22] Rajwade K.; Mickaliger M.; Stappers B. et al. Spectrotemporal Analysis of a Sample of Bursts from FRB 121102. *RNAAS*, 4:3, 2020. 1.3

[23] Gajjar V.; Siemion A.; Price D. et al. Highest Frequency detection of FRB 121102 at 4-8 GHz using the Breakthrough Listen Digital Backend at the Green Bank Telescope. *ApJ*, 863:2, 2018. 1.3

[24] Spitler L. G.; Cordes J. M.; Hessels J. W. T. et al. FRB 121102 Bursts Show Complex Time-Frequency Structure. *ApJL*, 876:14, 2019. 1.4

[25] Buckley J. H.; Bhupal Dev P. S.; Ferrer F. et al. Fast Radio Bursts from Axion Stars Moving Through Pulsar Magnetospheres. *PhysRevD*, 103, 2021. 2.1

[26] Brandenberger R.; Cyr B.; Varna Iyer A. Fast Radio Bursts from the Decay of Cosmic String Cusps. *ePrint*, 2017. 2.1

[27] Gu W. M.; Yi T.; Liu T. A Neutron Star-White Dwarf Binary Model for Periodically Active Fast Radio Burst Sources. *MNRAS*, 497:1543–1546, 2020. 2.1

[28] Dai Z. G.; Wang J. S.; Wu X. F. et al. Repeating Fast Radio Bursts from Highly Magnetized Pulsars Traveling through Asteroid Belts. *APJ*, 829:7, 2016. 2.1

[29] Tendulkar S. P.; Gil De Paz A.; Kirichenko A. Y. et al. The 60 pc Environment of FRB 20180916B. *ApJL*, 908:11, 2021. 2.1

[30] Cordes J. M.; Wasserman I. Supergiant Pulses from Extragalactic Neutron Stars. *MNRAS*, 457:232–257, 2016. 2.2

[31] Margalit B.; Berger E.; Metzger B. D. Fast Radio Bursts from Magnetars Born in Binary Neutron Star Mergers and Accretion Induced Collapse. *APJ*, 886:11, 2019. 2.2

[32] CHIME/FRB Collaboration. A Bright Millisecond-Duration Radio Burst from a Galactic Magnetar. *Nature*, 587:54–58, 2020. 2.2

[33] Marthi V. R.; Gautam T.; Li D. Z. et al. Detection of 15 Bursts from the Fast Radio Burst 180916.J0158+65 with the upgraded Giant Metrewave Radio Telescope. *MNRAS*, 499:L16–L20, 2020. 2.2

[34] Lam M. Pypulse. Astrophysics Source Code Library; record ascl:1706.011. 3.1

[35] Cordes J. M.; Rickett B. J. Diffractive Interstellar Scintillation Timescales and Velocities. *ApJ*, 507:846–860, 1998. 5.2, 5.2, 5.3, 5.4

[36] Macquart J. P.; Koay J. Y. Temporal Smearing of Transient Radio Sources by the Intergalactic Medium. *ApJ*, 776:13, 2013. 5.3, 5.3